

ARTICLE OPEN



Three-dimensional strain imaging of irradiated chromium using multi-reflection Bragg coherent diffraction

Ericmoore Jossou¹✉, Tadesse A. Assefa², Ana F. Suzana³, Longlong Wu³, Colleen Campbell⁴, Ross Harder⁵, Wonsuk Cha⁵, Kim Kisslinger⁶, Cheng Sun⁷, Jian Gan⁷, Lynne Ecker¹, Ian K. Robinson³ and Simerjeet K. Gill¹✉

Radiation-induced materials degradation is a key concern in limiting the performance of nuclear materials. The formation of nanoscale void and gas bubble superlattices in metals and alloys under radiation environments can effectively mitigate radiation-induced damage, such as swelling and aid the development of next generation radiation tolerant materials. To effectively manage radiation-induced damage via superlattice formation, it is critical to understand the microstructural changes and strain induced by such superlattices. We utilize multi-reflection Bragg coherent diffraction imaging to quantify the full strain tensor induced by void superlattices in iron irradiated chromium substrate. Our approach provides a quantitative estimation of radiation-induced three-dimensional (3D) strain generated at the microscopic level and predicts the number density of defects with a high degree of sensitivity. Such quantitative evaluation of 3D strain in nuclear materials can have a major impact on predicting materials behavior in radiation environments and can revolutionize design of radiation tolerant materials.

npj Materials Degradation (2022)6:99; <https://doi.org/10.1038/s41529-022-00311-8>

INTRODUCTION

Understanding degradation of structural materials under extreme environments is crucial for deployment of advanced nuclear technologies¹. Metallic alloys used as structural materials and fuels in nuclear reactors face extreme conditions including high doses of radiation, which significantly modify the residual stress and strain field in the material, directly impacting the performance of materials². Large quantities of fission gases are introduced into the metallic fuels and structural materials during reactor operation. These fission gases are insoluble in metal alloys, and rapidly precipitate to form bubbles, which nucleate and grow into voids, eventually leading to blistering³. Such blistering significantly alters the strain field and fatigue behavior of the structural materials, which is critical to understand for assessing and accurately predicting the materials' performance during in-service conditions as well as long-term performance for life extension. Elucidating the strain-generated and strain-induced modification of structural materials over the lifetime of nuclear materials remains an unsolved challenge, as current techniques cannot offer 3D imaging of the formation or interaction of defects, such as bubbles, and voids during dynamic processes. A promising approach is to infer the concentration of these radiation-induced defects, including voids, by measuring the lattice strain they cause in the crystal lattice of the structural materials. Lattice strain measures the structural deviation of a crystal from the ideal bulk state and is defined as the spatial derivative of the displacement of the material from an ideal lattice⁴.

Chromium is an important alloying element for the development of accident tolerant cladding tubes in light water reactors^{5,6}, which are subjected to extreme environments during reactor operation. Typical operating temperatures are in the region of 588–628 K⁷, with a heat rate of 15–25 kW/m and a neutron flux

accumulation of several displacements per atom (dpa)/year⁸. Chromium's relatively high melting point (1833–1882 °C)⁹, high thermal conductivity¹⁰, reasonable neutron capture cross-section¹¹, good hardness, wear resistance¹², and excellent corrosion resistance^{13,14} make it a suitable coating material for improving the corrosion resistance of currently used 'zircalloy' cladding tubes^{15–17}. Hence, understanding lattice-induced strain and defect density in chromium is important and can be easily adapted to understand radiation-induced strain in popular bimetallic 80 wt% Ni–20 wt% Cr (Ni–20Cr) and structural materials, such as Inconel and Hastelloy. A significant amount of damage accumulates in structural materials during the lifetime of reactor operation. Besides neutron-induced cascade damage, transmutation produces varying isotopes of various alloying elements including chromium¹⁸. The high radiation doses coupled with the high temperature during reactor operation leads to degradation of structural material properties, resulting in hardening, embrittlement, creep, and swelling^{19–21}. Further, the radiation-induced defects and associated strain can alter performance of structural materials, such as offsetting the fatigue loading, thereby accelerating material deformation by reducing the fatigue deformation cycle, limiting the service life of a nuclear reactor^{17,22–25}. Hence, fundamental understanding of radiation-induced defects and associated strain is critical to addressing the long-term performance of structural materials and life extension issues of nuclear reactors.

Radiation-induced defects and the subsequent cascades within chromium have been investigated using both computational methods²⁶ and experimental techniques^{27–29}. For instance, Maier et al. used in situ ion irradiation and TEM to study cold spray deposited Cr coatings for use in accident tolerance fuel cladding. The severely plastically deformed microstructure of the cold spray

¹Nuclear Science and Technology Department, Brookhaven National Laboratory, Upton, NY 11973, USA. ²Stanford Institute for Materials and Energy Sciences, SLAC National Accelerator Laboratory, Menlo Park, CA 94025, USA. ³Condensed Matter Physics and Materials Science Department, Brookhaven National Laboratory, Upton, NY 11973, USA. ⁴Department of Nuclear Science & Engineering, Massachusetts Institute of Technology, Cambridge, MA 02139, USA. ⁵Advanced Photon Source, Argonne National Laboratory, Lemont, IL 60439, USA. ⁶Center for Functional Nanomaterials, Brookhaven National Laboratory, Upton, NY 11973, USA. ⁷Idaho National Laboratory, Idaho Falls, ID 83415, USA. ✉email: ejossou@bnl.gov; gills@bnl.gov

deposited Cr delayed the onset and growth of radiation-induced defects when compared to an annealed coating simulating bulk Cr, which could be explained by lower defect density and smaller loop size in cold spray deposited Cr as compared to bulk Cr. For example, the number of spot type defects in the bulk Cr sample at 0.1 displacements per atom (dpa) is similar to the number of the defects in the cold spray deposited Cr sample at 0.7 dpa. Further, the dislocation loop size in bulk Cr was 60% bigger. Both these parameters demonstrate the superior radiation resistant ability of cold spray Cr as compared to bulk Cr, emphasizing the strong potential of cold spray Cr coatings to strengthen the performance of accident tolerant claddings¹⁶.

Meanwhile, Jiang et al. investigated the cavity nucleation and growth in bcc α -Cr under single, dual, and triple ion beam irradiations using combined experimental and computational methods. The implantation of hydrogen and helium leads to a large amount of volume swelling and further worsens chromium hardening and embrittlement. This is because the co-implantation of helium with iron enhances cavity nucleation, while the co-implantation of hydrogen with iron leads to significant cavity growth. Hydrogen also serves to accelerate cavity nucleation in the presence of helium implantation. Under triple beam irradiation using Fe^{++} , H^+ , He^{++} , both the size and density characteristics of the cavities appear to be controlled primarily by the helium component²³. These studies reveal the synergistic effect of triple beam irradiation, where the presence of helium increases the maximum number of hydrogen atoms that can be captured by a vacancy from 6 to 9, demonstrating that degradation due to radiation in Cr can be controlled and mitigated by controlling irradiation conditions.

More recently, Ryabikovskaya et al. studied the radiation response of pure Cr where Cr was irradiated with 5 MeV Fe ion to investigate void swelling behavior over the temperature range of 450–650 °C using TEM analysis. The void swelling peaks at 550 °C, reaching ~2% swelling after 50 peak dpa irradiation. The void alignment along the $\langle 111 \rangle$ axial direction was observed, which implies the formation of void superlattice²⁹. Also, it was observed that pure chromium swells at a much lower rate of ~0.03–0.04%/dpa (up to 120 local dpa) as compared to pure iron with a post-transient swelling rate of ~0.2%/dpa. Such low swelling rate for Cr is encouraging for potential use of Cr coatings for improving accident tolerance; however, additional studies need to be conducted over a wider range of dpa rates for recommending Cr coating with confidence for reactor applications. Also, most of these studies are limited to thin foils for TEM studies, which means defects may be lost to nearby surfaces that act as strong defect sinks, thereby reducing the apparent defect density and making the sample under study not representative of the bulk sample^{30,31}. Furthermore, 3D strain imaging using TEM samples becomes difficult for higher damage levels due to defect-defect interactions.

BCDI is a very powerful method for 3D characterization of radiation-induced lattice strain, as it has the combination of 10–20 nm spatial resolution in 3D, high strain sensitivity, and allows us to probe thicker materials because of the large penetration depth offered by hard X-rays during measurement³². In BCDI, data is collected by illuminating the microcrystal sample with a coherent, monochromatic X-ray beam while satisfying the Bragg condition for a given crystallographic reflection. The sample is then rocked through the Bragg condition, and a series of 2D diffraction patterns are collected in the far-field limit. After stacking all the recorded 2D diffraction patterns into the 3D, the collected diffraction pattern can be inverted using phase retrieval algorithms³³ to give the 3D real-space information of the measured sample image with complex values. The sample size is restricted to sub-micron crystals, owing to the sub-micron longitudinal coherence lengths in the hard X-ray regime at current synchrotron sources. One BCDI measurement gives one

component of the displacement field. Obtaining all three Cartesian components of the displacement vector requires at least three measurements at non-planar Bragg reflections, such that the full lattice strain tensor can be determined^{34–36}. The use of focused ion beam (FIB) milling has allowed for the fabrication of BCDI strain microscopy samples, which makes it possible to investigate radiation-induced strain field at a length scale that is not traditionally accessible with electron microscopic techniques, such as transmission electron microscopy (TEM)³⁵.

In this work, we utilize multi-reflection BCDI to elucidate radiation-induced strain in 5 MeV Fe ion irradiated chromium. We systematically study void-induced strain where instead of being distributed randomly, the voids are observed to self-organize periodically in space with a body centered cubic lattice symmetry under the carefully chosen irradiation conditions for our study. The voids replicate the symmetry and crystallographic orientation of the host matrix and form a lattice called 'the void lattice'. The presence of the void lattice not only has a dramatic impact on the toughness, ductility, dimensional stability, and thermal performance but also accounts for the improved swelling behavior, resulting in superior longevity of structural materials in nuclear reactors³⁷. Unlike previous TEM analysis, our approach of using BCDI allows us to directly probe the full strain field associated with the sub-micron implantation-induced voids layer and makes it possible to resolve the spatial heterogeneity of the implantation-induced strain, which provides fundamental understanding of radiation-induced defects and associated microstructure in 3D. Such detailed understanding of radiation-induced strain in 3D and quantitative prediction of number density of defects enables precise prediction of degradation inventory directly informing models predicting materials performance.

RESULTS

Data collection

Chromium sheets of 99.7% were purchased from American Elements Inc. The sample was irradiated with 5 MeV Fe ions that modified a ~2 μm thick surface layer (see Methods) and generated neutron-like collision cascade damage. This is relevant because during fission reactor operation, fast neutrons are generated by the fission process. Fast neutron irradiation under the right temperature conditions can lead to void formation and growth, which then leads to swelling over the lifetime of the reactor. Our use of Fe ion irradiation therefore effectively mimics neutron bombardment. The stopping and range of ions in matter (SRIM) code³⁸ was used to predict the damage profile as shown in Fig. 1a. Finally, using Focused Ion Beam (FIB) milling, a cross-section sample was extracted from the bulk, and a region of $3 \times 2 \times 2 \mu\text{m}^3$ was thinned to $1.5 \times 1.5 \times 1.5 \mu\text{m}^3$ and mounted on a silicon wafer as shown in Fig. 1b, c.

The experiment was performed at 34-ID-C at Advanced Photon Source, Argonne National Laboratory, USA. A double crystal monochromator was used to select the energy to 9.0 keV and Kirkpatrick–Baez mirrors were used to focus the beam to $600 \times 600 \text{ nm}^2$ as shown in Fig. 2a (see Methods section for full details). A multi-reflection BCDI dataset consisting of four Bragg reflections, (101), (011), ($0\bar{1}1$), and ($\bar{1}01$), was measured as the sample was rocked through the Bragg condition to collect over-sampled 3D data in reciprocal space. Plots of the coherent diffraction patterns collected near the (101), (011), ($0\bar{1}1$), and ($\bar{1}01$) Bragg reflections from the same sample are shown in Fig. 2(b)–(e). The diffraction peaks are strongly speckled on the detector because of the high coherence of the beam and high stability of the setup used at the 34-ID-C beamline. While the overall shape of each peak is the same, the distribution of speckles within it is

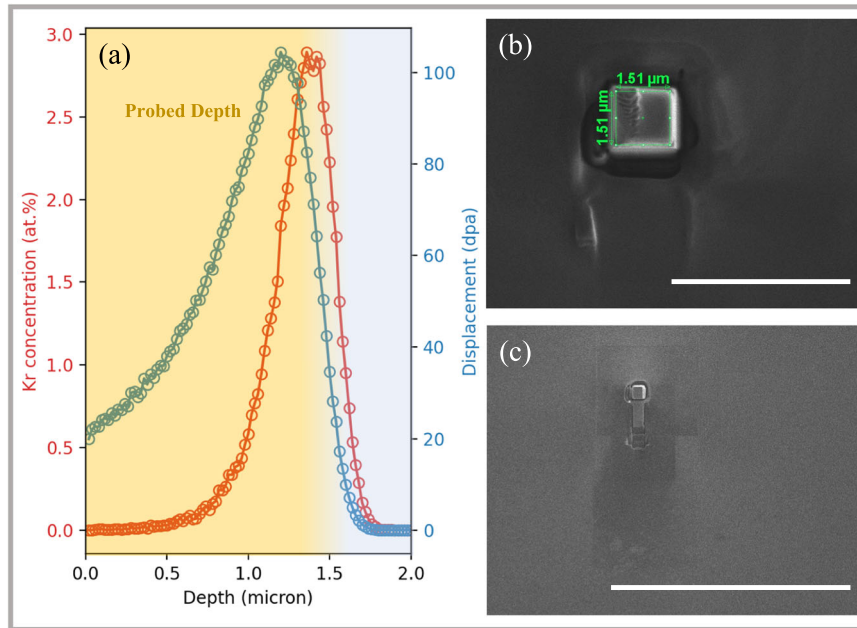


Fig. 1 The ion implantation profile and the focused ion beam assisted sample liftout. **a** Plot of the expected dpa and injected ion concentration as a function of depth after 5 MeV Fe ion implantation. **b** SEM micrograph of the multi-reflection BCDI strain microscopy lift-out. Here, the initial rectangular-shaped platinum cap marks the lift-out region, and the approximate position of the BCDI sample is shown. The scale bar shown corresponds to 5 μm . **c** SEM image of the finished sample with the location of the implanted layer mounted on a silicon wafer. The scale bar shown corresponds to 40 μm .

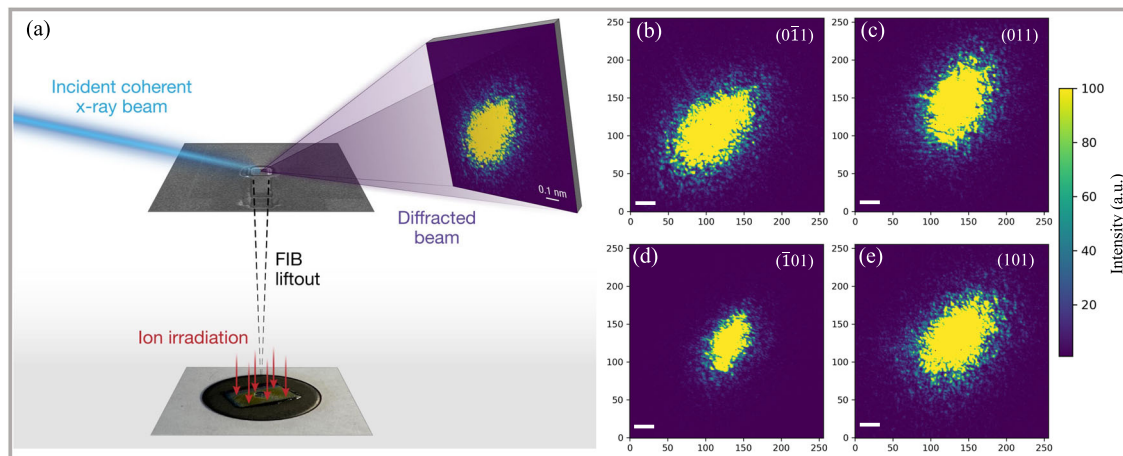


Fig. 2 Schematic of the BCDI experiment and 2D diffraction patterns. **a** Diagram of the experimental setup used the BCDI measurements in this work. Coherent X-rays from a synchrotron source are directed to the sample using a Kirkpatrick–Baez mirror (not shown) and are diffracted by the Fe ion irradiated chromium crystal. The constructive interference patterns of the diffracted X-rays are recorded while rocking the sample in theta in steps of about 0.001° about the Bragg condition for four non-coplanar Bragg's peaks, effectively measuring the three-dimensional Bragg peak. When the Bragg peak is sufficiently over-sampled, it is possible to apply established phase retrieval algorithms to solve for the complex wave function of the scattered X-rays. **b–e** Central slices of the 3D coherent X-ray diffraction pattern for each reflection measured on the ion-implanted sample. The scale bar was calculated using the relationship $2\pi p/\lambda d$, where $\lambda = 0.138 \text{ nm}$ is the wavelength, $p = 55 \mu\text{m}$ is the detector pixel size, and $d = 2.0 \text{ m}$ is the sample to detector distance. The scale bar shown corresponds to 0.1 nm^{-1} .

different due to the heterogeneity of the radiation-induced defect distribution.

Details regarding the recovery of the real-space images using phase retrieval algorithms can be found in supplementary methods and the computation of the strain field can be found in the supplementary discussion. The strain fields were calculated by differentiating the displacement field with respect to the sample-frame directions x , y , and z . The full strain and rotation tensors are presented in a 3×3 format as shown in Table 1.

Three-dimensional imaging of the defects

The 3D morphology of the sample, recovered from each crystal reflection, is shown in Fig. 3a, rendered as a semi-transparent isosurface of the Bragg electron density (BED) (see supplementary discussion for movie 1 showing an animated version of Fig. 3a). The spatial resolution of the reconstruction was estimated using the spherically averaged phase retrieval transfer function (PRTF)³⁹ and ranges from 29 nm to 32 nm. The procedure for the PRTF is available in supplementary Fig. 1.

The morphology of the sample, recovered from different reflections, is consistent with the sample dimension from the Scanning Electron Microscopy (SEM) image in Fig. 1(b)–(c). Careful inspection of the reconstructed images shows a network of voids and possible dislocation loops due to the ion implantation. It is important to note that there is no distinct unimplanted region in the sample, which is consistent with SRIM simulation that suggests a peak damage of 100 dpa at a depth of $\sim 1.3 \mu\text{m}$ while the damage accumulation within the $1.4\text{--}1.5 \mu\text{m}$ depth reduces. It is important to note that the reconstructed morphology consists of the BED, which shows the crystal morphology, and the phase, which represents the projection of the lattice distortions within the crystal onto the direction of the measured Bragg peak^{33,40}. The BED is the amplitude of the image measured at a specific Bragg peak. Its value tells us how strongly that part of the sample contributes to the Bragg peak.

To completely characterize the strain associated with defects in a small crystal structure, three or more independent Bragg peaks must be measured³⁴. This also ensures that most defects presented are discovered, as defects in certain orientations do not affect certain Bragg reflections. For example, the different Bragg's reflections in Fig. 3a show a different distribution of voids and dislocations in the Fe-irradiated chromium. A careful inspection of (011) and $(\bar{0}\bar{1}1)$ reflections shows a layer of denuded zone as highlighted by the black broken lines. A superimposition of the different reflections gives a complete distribution of the defects as shown in Fig. 3b. Microstructural evolution in irradiated Cr is a complex process that covers large time and length scales, ranging from individual atomic events, such as point defect generation during radiation cascades on the scale of

femtoseconds and nanometers, to diffusion and accumulation of vacancies into voids at nanometer to micron scale as observed in ion irradiated chromium. Previous defects in BCDI measurements showed that dislocations appear as pipes of missing electron density⁴¹ while vacancies and voids are denoted by clusters of flake-like features⁴². The reason is that large lattice strains near the defects (in our case voids) lead to a scattered intensity that cannot be captured by the numerical aperture of the detector, causing an apparent loss of electron density at the region where the defects occur. Hence, by superimposing the electron density recovered from all four measured crystal reflections, voids, which appear as clusters of vacancies, can be observed throughout the sample as shown in Fig. 3.

To visualize the distribution of the defect features more clearly, we show the 2D iso-surfaces of the BED generated in the laboratory cartesian coordinate frame such that z is along the beam direction while x and y are transverse and vertical to the beam, respectively. The BED shows the crystal morphology and the phase and corresponds to the projection of the lattice distortions within the crystal onto the direction of the measured Bragg peak. Its value can drop if the sample region becomes disordered or if it changes orientation to no longer satisfy the Bragg condition. In Fig. 4, voids in the ion irradiated specimens appear as missing electron density in the images. It has been previously reported that injected interstitials almost always suppress void formation in both pure metals and alloys in injected region^{43–45}. As for the near-surface region, a high density of voids exists immediately beneath the surface with no denuded zone. Note that some erosion of the BCDI microscopy sample surface during thinning is observed. This may have removed the void denuded zone at the surface, if indeed originally there was one present. However, such a removal does not cause a noticeable change in the swelling profile.

Previous TEM analysis shows void alignment in chromium samples with similar irradiation conditions as used in this work. The voids are aligned along the vertical direction of the image. Void superlattice are clearly visualized in an enlarged scanning TEM image under optimized tilting at the dose level²⁹ used for current study. However, the void distribution shown in Fig. 4 does not show clear periodicity due to the limited spatial resolution of

Table 1. Lattice strain tensor components and lattice rotations. The representation of lattice strain and rotation in Fig. 5 follow this layout.

$\epsilon_{xx} = \frac{\partial u_x}{\partial x}$	$\epsilon_{xy} = \frac{1}{2} \left(\frac{\partial u_x}{\partial y} + \frac{\partial u_y}{\partial x} \right)$	$\epsilon_{xz} = \frac{1}{2} \left(\frac{\partial u_x}{\partial z} + \frac{\partial u_z}{\partial x} \right)$
$\omega_z = \frac{1}{2} \left(\frac{\partial u_y}{\partial x} - \frac{\partial u_x}{\partial y} \right)$	$\epsilon_{yy} = \frac{\partial u_y}{\partial y}$	$\epsilon_{yz} = \frac{1}{2} \left(\frac{\partial u_y}{\partial z} + \frac{\partial u_z}{\partial y} \right)$
$\omega_y = \frac{1}{2} \left(\frac{\partial u_x}{\partial z} - \frac{\partial u_z}{\partial x} \right)$	$\omega_x = \frac{1}{2} \left(\frac{\partial u_z}{\partial y} - \frac{\partial u_y}{\partial z} \right)$	$\epsilon_{zz} = \frac{\partial u_z}{\partial z}$

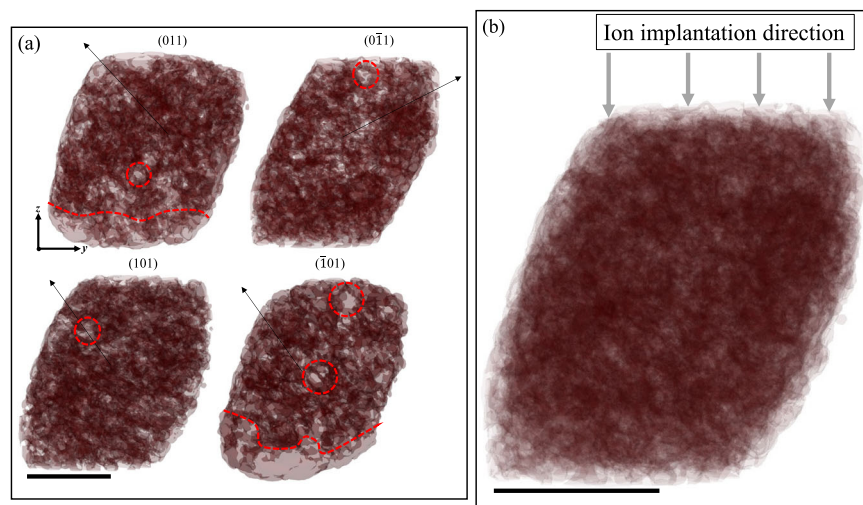


Fig. 3 3D visualization of defects structures. The particle shape is shown as a semi-transparent isosurface, and the defects clusters are shown in brown color while defects free region are highlighted in red circles and lines. **a** Semi-transparent 3D rendering of the electron density amplitude recovered from BCDI measurements of four different reflections. The (011) and $(\bar{0}\bar{1}1)$ reflections show a layer of a denuded zone as shown by the red broken lines. The Bragg vector direction for each reflection is indicated by the black arrows. The scale bar is $1.0 \mu\text{m}$ long in each case. **b** The defects distribution across the sample is well visualized by the superimposition of each Bragg's reflection on the recovered sample morphology.

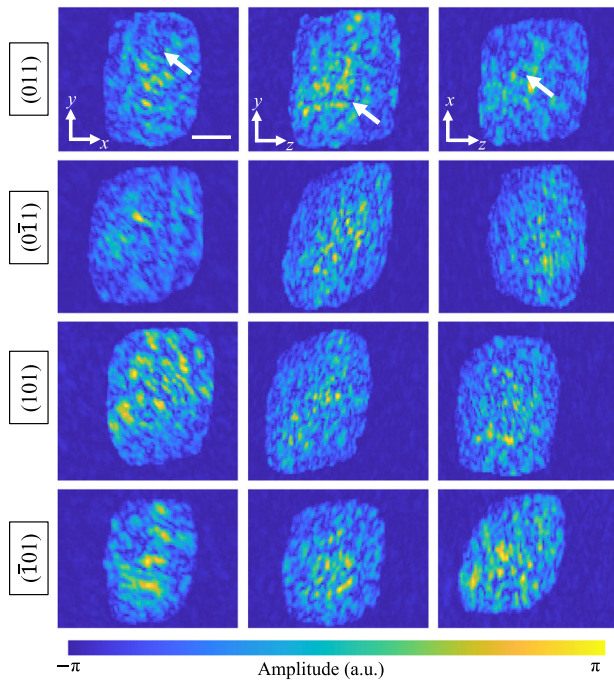


Fig. 4 Slices showing the electron density of irradiated chromium sample with the (011), (01̄1), (101), and (1̄01) Bragg's reflections. Representative voids and dislocations are highlighted by white arrows featuring a low-amplitude core denoted as missing electron density. The scale bar is 1 μm .

~ 30 nm of the BCDI measurement. While it is counterintuitive that an imaging experiment with ~ 30 nm spatial resolution is sensitive to atomic-scale defects such as dislocations and voids. In our case, BCDI is sensitive to defects such as voids and dislocations through its strain field sensitivity⁴⁶. This is illustrated by the relationship between the continuum representation of the crystal, $\varphi(r)$, and the diffraction intensity, $I(q)$ in the far-field under a perfectly coherent illumination and in the kinematical scattering approximation given by $I(q) \approx |\mathcal{F}(\varphi(r)e^{iQ \cdot u(r)})|^2$. Here, r and q are the real and reciprocal space coordinates, respectively, \mathcal{F} is the Fourier transform, Q is the measured Bragg peak, and $u(r)$ is the vector displacement field that is a continuum description of how the atoms are displaced from their equilibrium positions⁴⁷.

Although the FIB sample preparation between the TEM and BCDI are comparable, BCDI is more sensitive to damage layers as compared to TEM as shown by Hofmann et al.⁴⁷. Hence, such a microstructural disparity between TEM and BCDI can be attributed to FIB-induced damage^{48,49} in BCDI study. A recent study showed that even at a low dose of Ga^+ milling, large lattice strain due to microstructural changes can be introduced into the sample³³. In the current work, low energy milling (acceleration voltage below 2 kV) was utilized during the chromium lift-out to remove the shallow surface damage introduced by previous high-energy milling steps³⁵. Careful sample preparation was done to minimize FIB-induced damage, which was further factored into the strain analysis in the implanted layer of the chromium sample.

Correlating strain distribution with void density

The formation of radiation-induced defects and defects associated with gas implantation gives rise to the volumetric expansion (swelling) of materials⁵⁰. The magnitude of the lattice strain exhibits a complex pattern of strain variation as a function of dose and temperature⁵¹. The strain values were transformed to an orthogonal sample space, x, y, z , where the x -axis is along the y - z direction, the y -axis along x - z , and z -axis along x - y , as shown in

Fig. 5(a). The reconstructed strain tensor of the Fe-irradiated chromium sample is shown in Fig. 5(b)–(d). The in-plane strain components are generally small compared to the out-of-plane strain, which is consistent with ion irradiation in tungsten⁴² and Fe–Cr alloys⁵². Regions of swelling and contraction are observed throughout the Cr substrate, which suggests the absence of unimplanted region. This is consistent with the SRIM profile where the damage is ~ 38 dpa even at a depth of 1.5 μm . In specific terms, the average value of the strain field is $\sim 3.0 \times 10^{-4}$ while the minimum and maximum strain are -3.0×10^{-3} and 5.5×10^{-3} , respectively. This is indicative of strain heterogeneity within the Fe implanted chromium substrate. Such observation of strain heterogeneity can be attributed to point defects, such as vacancy clustering⁵³, which lead to void formation and further void-induced strain in the chromium substrate.

The heterogeneous nature of the strain is supported by the long stripes of tensile regions that run through the ϵ_{xx} , ϵ_{yy} and ϵ_{zz} components of Fig. 5(b)–(d). Alongside the tensile regions, an existence of compressive type strains is observed, such that dislocation features occur at the junction where tensile and compressive strains meet. The strain variation observed here is supported by previously reported atomic-scale simulations where the defects microstructure is attributed to the spatially changing strain and stress field induced after heavy ion irradiation⁵⁴. The strain sensitivity and accuracy of BCDI for a 5 MeV Fe ion irradiated chromium are supported by recent work by Phillips et al. where they showed remarkable agreement in strain in two tungsten samples irradiated with implantation energies differing by an order of magnitude. The 2 MeV sample was measured with BCDI while the 20 MeV strain was mapped with differential aperture X-ray microscopy. The strain sensitivity of BCDI measurements is on the order of $\sim 2 \times 10^{-4}$ from previous measurements^{32,36}, demonstrating high accuracy of BCDI-based strain mapping.

Since the average lattice strain values for each depth are positive implies that some interstitial defects are present in the sample. We therefore assumed that all dislocation loops are of interstitial and vacancy types with $\frac{1}{2}\langle 111 \rangle$ Burger's vector, which is consistent with the most recent work on irradiated chromium⁵⁵. The magnitude of the phase jumps ($\Delta\psi_{hkl}$) due to a dislocation with Burger's vector \mathbf{b} observed in a given hkl reflection is $\mathbf{b} \cdot \mathbf{q}_{hkl}$ where \mathbf{q}_{hkl} is the scattering vector associated with the (011), (01̄1), (101), and (1̄01) crystal reflections respectively. As a demonstration, \mathbf{q}_{011} is given by $(2\pi/a)[011]$, where a is the lattice constant. The computation of the dislocations with Burger's vector \mathbf{b} in crystal reflections with scattering vector \mathbf{q}_{hkl} suggest a visible dislocation network denoted by phase jumps in the range of -2π to 2π as shown in Table 2.

We excluded the formation of $\frac{a}{3}\langle 112 \rangle$ loops in our work since Cui et al. suggest that their formation is energetically unfavorable in bcc Cr at temperature of 550 °C⁵⁵. However, Bryk et al. reported $\frac{a}{3}\langle 112 \rangle$ loops on {111} planes and $\frac{a}{3}\langle 111 \rangle$ loops on {110} planes at 650 °C using TEM. The formation of $\frac{a}{3}\langle 112 \rangle$ loops at higher temperatures is due to the interaction of two Shockley partial dislocations according to the reaction $\frac{a}{2}[111] + \frac{a}{6}[-1-11] \rightarrow \frac{a}{3}\langle 112 \rangle$, the so-called '111 mechanism'⁵⁶.

The formation of radiation-induced planar defect agglomerates, such as voids and loops, and their evolution into 3D defect agglomerates, such as voids and potential void ordering in irradiated chromium, accounts for the swelling observed in chromium substrate. In addition, swelling has been attributed to the preferential absorption of self interstitial atoms (SIAs) to dislocation loops in metals, based on the dissociation of vacancies from clusters and their diffusion in the matrix^{25,29,57}. Lattice strain is the direct response of the net contributions of the positive relaxation volume from interstitial defects and negative relaxation volume from vacancies. Therefore, it is sensitive to the population of different defect types, including extended defect structures rather than the total defect

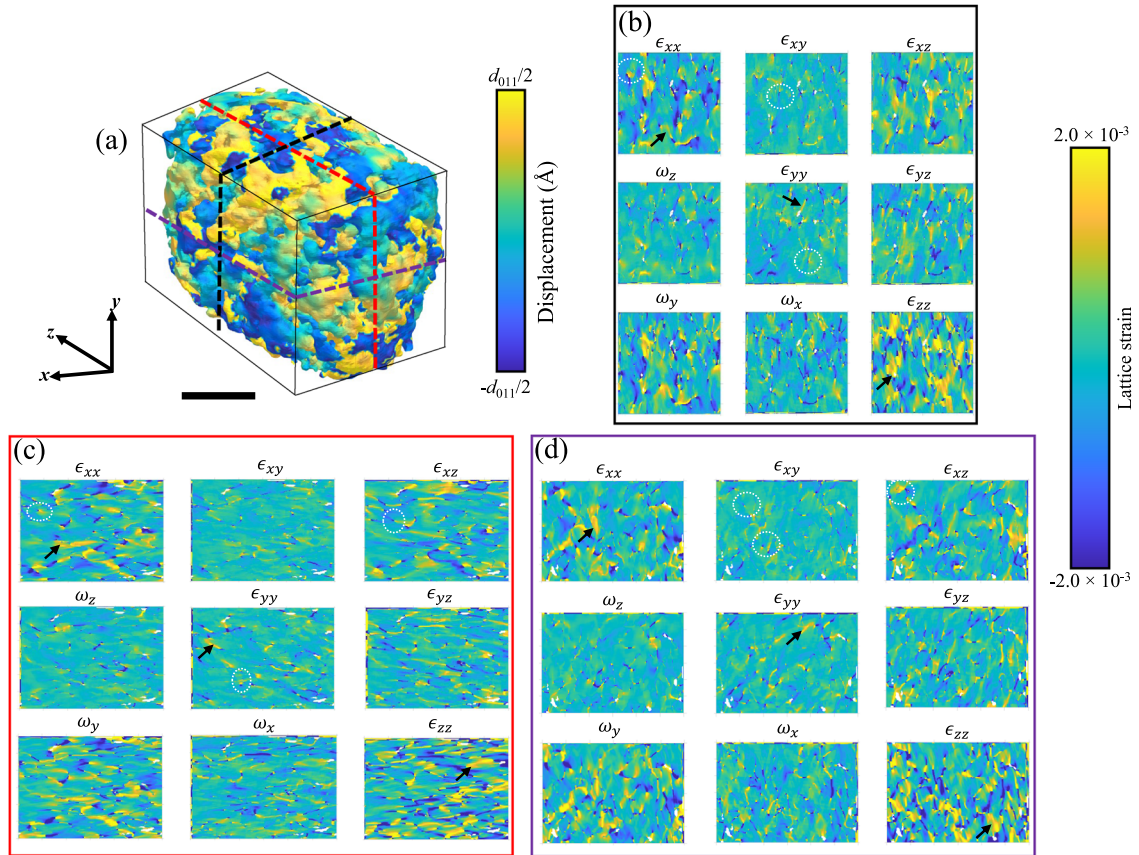


Fig. 5 Reconstructed strain in irradiated chromium crystal. **a** Rendering of the reconstructed lattice displacement with magnitude $|u(r)|$ in the $[101]$ direction. The superimposed arrows indicate the directions of x , y , and z -axes with the corresponding crystallographic directions. Also shown are three sections through the crystal for which strains are shown in (green, red, and purple). Six strain tensors and three rotation tensors components are plotted on the **b** x - y plane **c** y - z plane **d** x - z plane of the crystal. Representative tensile stripes are shown with black arrows while dislocation loops are shown using white circles. All scale bars correspond to $1.0 \mu\text{m}$.

Table 2. Visibility of dislocations with Burger's vector \mathbf{b} in crystal reflections with scattering vector \mathbf{q}_{hkl} .

\mathbf{b}				
\mathbf{q}_{hkl}	(011)	(0 $\bar{1}$ 1)	(101)	($\bar{1}$ 01)
$\frac{a}{2}[111]$	2π	0	2π	0
$\frac{a}{2}[\bar{1}11]$	2π	0	0	2π
$\frac{a}{2}[\bar{1}\bar{1}1]$	0	2π	2π	0
$\frac{a}{2}[11\bar{1}]$	0	-2π	0	-2π
$\frac{a}{2}[\bar{1}\bar{1}\bar{1}]$	0	2π	0	2π
$\frac{a}{2}[\bar{1}1\bar{1}]$	0	-2π	-2π	0
$\frac{a}{2}[\bar{1}\bar{1}1]$	-2π	0	0	-2π
$\frac{a}{2}[\bar{1}\bar{1}\bar{1}]$	-2π	0	-2π	0

population⁵². Therefore, we can accurately estimate the population of the dominant defects, which are voids and Frenkel pairs from the measured lattice strain tensor. The measured lattice swelling suggests that not all SIAs are lost to sinks, such as sample surfaces or dislocations, but rather that a population of SIAs is retained within the damaged substrate layer. The ratio of retained vacancies to SIAs cannot be determined. However, we can estimate the defect density, assuming retention of a population of Frenkel pairs along with a condition that there is equal number of vacancies and SIAs.

The average value of the lattice strains measured from the Fe-irradiated Cr sample in this study are positive, which explain the swelling of Cr substrate, suggesting that interstitial defects have been retained in chromium substrate after Fe irradiation. We can use the measured lattice strain to estimate the equivalent Frenkel pair density in the materials. By considering the relative relaxation volumes ($\Omega_r(V)$) of defects in pure Cr, the measured strain can be used to calculate the defect density in the material, by using Eq. 1⁵⁸:

$$\epsilon_{zz} = \frac{(1 + \nu)}{3(1 - \nu)} \sum_A n(V)\Omega_r(V), \quad (1)$$

where ϵ_{zz} is the measured out-of-plane strain, ν is the Poisson ratio and is 0.21 for pure Cr⁵⁹ while $n(V)$ and $\Omega_r(V)$ are, respectively, the defects number density and relative relaxation volume for defect type V . Furthermore, since the dominant defects are voids, we have estimated the average number of vacancies per void (a), assuming a spherical shape of the voids, which is consistent with the microstructural features of chromium irradiated with Fe at the same temperature used in this study²⁹. The value of a is related to the void radius using Eq. 2⁶⁰:

$$a = \frac{4\pi R_v^3}{3\Omega_r}, \quad (2)$$

where R_v denotes the average void radius and Ω_r the atomic relaxation volume.

The $\langle 100 \rangle$, $\langle 110 \rangle$ and $\langle 111 \rangle$ are the predominant dislocation defects configurations observed in Cr^{59,61}. Hence, for one SIA, the relative relaxation volume (Ω_r) is 1.61, 1.43, and 1.34 for the $\langle 100 \rangle$,

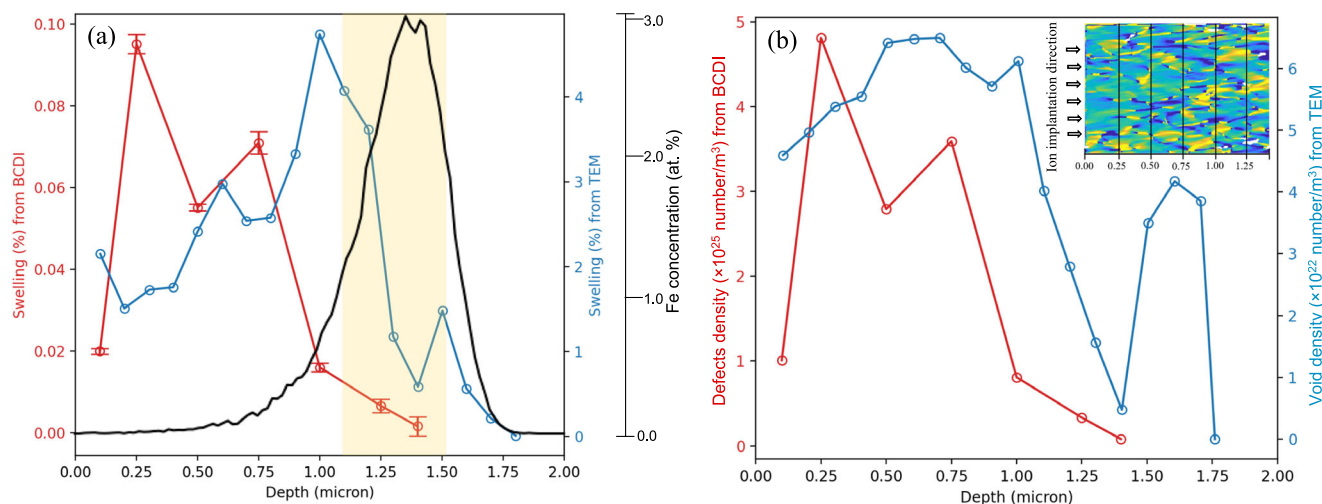


Fig. 6 Swelling and defects density profile estimated from lattice strain. **a** SRIM-predicted Fe implant distribution for 100 peak dpa irradiation superimposed on the swelling profile as a function of depth in pure chromium irradiated at 550 °C to 100 peak dpa. The box indicates the region of maximum compositional alteration by Fe implantation. **b** void densities as a function of depth. The inset shows the depth at which the strain data are averaged for each irradiation depth. Note—The scale bar for swelling from BCDI and TEM are different and are adjusted for best visualization of the trends.

$\langle 110 \rangle$, and $\langle 111 \rangle$ configurations, respectively, while the Ω_r of an isolated vacancy defect is -0.41 ⁵⁹. It is assumed that there is no loss of interstitial atoms in the sample and the number of vacancies is equivalent to the number of interstitial atoms. This allows us to estimate the number density of the Frenkel pairs. It has been shown that interstitial clustering will result in decrease in relaxation volume per defect which in turn accounts for equivalent decrease in the Frenkel pair density⁵⁸. However, the void formation observed in the chromium substrate is evidence of vacancies clustering at 550 °C used for irradiation of Cr substrate. Therefore, to account for the clustering effects, we calculated the average number of vacancies per void (a) using Eq. 2. Using an average void diameter of 8.1 ± 2.1 nm at 550 °C²⁹, the a is $\sim 25,000$ vacancies per void. This is then used to scale the volumetric number density of equivalent vacancies to arrive at the void number density.

Previous studies suggest that void and irradiation ion concentration is depth dependent^{62–64}. The void density follows the same trend as suggested by the work of Ryabikovskaya et al.²⁹. However, the estimation using X-ray diffraction-based strain data is 3 orders of magnitude higher than the TEM-based results as shown in Fig. 6a. While the void densities at ~ 1.4 μm are locally reduced to almost zero from TEM, strain data shows the corresponding densities to be $\sim 10^{22}$ number/ m^3 . The reduced void density occurs at the Fe ion irradiated region. It has been established that a strong void suppression occurs at relatively high damage level. Meanwhile, the volumetric number density of equivalent Frenkel pairs is $0.1\text{--}1.34 \times 10^{26}$ number/ m^3 assuming all interstitial defects are of $\langle 100 \rangle$ in nature; while in the case where all interstitial defects are assumed to be $\langle 111 \rangle$ in nature, the corresponding number density of equivalent Frenkel pairs is between $0.1\text{--}1.61 \times 10^{26}$ number/ m^3 . It is important to note that these estimates provide a lower and upper bound of the number density of the Frenkel pairs present in the Fe-irradiated Cr substrate since the minimum and maximum strain values are used in the calculations.

To further demonstrate the strain sensitivity of BCDI and account for the disparity in the void density reported here, we show a comparison between the depth dependent strain data (swelling) from TEM and BCDI in Fig. 6a. The swelling profiles from TEM and BCDI show a similar trend as function of depth where swelling first increases and more importantly decreases

significantly in the highlighted region. It should be noted that scale of axis was adjusted to clearly demonstrate this trend. Further, the swelling observed by BCDI is about 2 orders of magnitude lower across the depth with respect to the TEM measurement up until a depth of ~ 1.5 μm . The Fe distribution from SRIM prediction as a function of depth is superimposed on the swelling profile. Swelling is greatly suppressed in the highlighted region, which coincides with the maximum Fe concentration. Such decrease in swelling of chromium substrate is likely due to the presence of injected interstitials, which have been reported^{24,25,65} to suppress swelling of metallic substrates in previous studies. The overall swelling profiles suggest that the distribution of Fe from SRIM is reasonably accurate and in agreement with radiation-induced swelling predicted by both TEM and BCDI strain analysis.

In Fig. 6b, we see that defect number density for TEM is 3 orders of magnitude lower than BCDI-based defect density. This difference in defect number densities between TEM and X-ray diffraction-based strain measurements may be due to the loss of defect loops to the surface sinks in TEM samples. Furthermore, contributions from defects below the detection limit of TEM are not accounted for while X-ray diffraction-based measurements are sensitive to the contribution from all defects in the sample⁴². The observed discrepancies are consistent with a recent study by Phillips et al., which showed that the number density of Frenkel pairs in implanted tungsten can be estimated as ~ 450 appm and ~ 640 appm for 20 MeV and 2 MeV preparations, respectively, while TEM analysis has shown number of defect density is typically in the range of 10–250 appm⁴². Another study on irradiated Fe–Cr alloys shows that defects density increases with increase in dpa level when using TEM data whereas the defect density calculated from X-ray diffraction-based strain data is proportional to the natural logarithm of damage⁵². Our studies demonstrate that BCDI offers a more accurate estimation of strain in Fe-irradiated chromium, which is consistent with a previous report⁴², which clearly shows that TEM measurements underestimate the defect density particularly at lower damage levels where the defects are smaller.

The disparity in defect densities between TEM and lattice strain measurements is mainly due to contributions from defects below the sensitivity limit of TEM^{66,67}. This assertion is supported by atomic-scale simulations that showed that small clusters of 3D

self-interstitial atoms with C15-type structure in bcc iron⁶⁸ is the most stable configuration but due to their small size of <1.5 nm diameter makes them invisible to TEM⁶⁶. However, the presence of these small clusters would still impart measurable strain to the material⁶⁹, contributing to the discrepancy between the measured strain and the defect density measured in TEM. Recent microdiffraction-based strain analysis reported ~2 order of magnitude disparity in the defect density in comparison to TEM⁵² while Hirst et al. used differential scanning calorimetry to measure defect densities which is 5 times greater than those determined using TEM in neutron irradiated titanium⁷⁰. It is important to note that the correlation between lattice strain and defect contrast in TEM offers a promising approach to fully describe the irradiation-induced defect population at low damage levels. Furthermore, underestimating the defect density prevents TEM from accurately determining the corresponding change in properties. For instance, Weiß et al. show a factor of 2 between measured and calculated change in hardness for neutron irradiated EUROFER97⁷¹. Meanwhile, Reza et al. report the same discrepancy between Transient Grating Spectroscopy (TGS)-measured and TEM-determined thermal diffusivity for self-ion irradiated tungsten⁷². It is important to note that when Reza et al. included small defects from molecular dynamics (MD) simulations, the combination of the TEM and MD data matches TGS measurements. This result confirms the theory that point defects play a significant role in the thermal diffusivity of a material and further reinforces the need to accurately characterize small defects in order to evaluate irradiation-induced changes in properties. Hence, the difference in the magnitude of swelling between TEM and BCDI estimates is justified.

DISCUSSION

BCDI-based strain mapping provides valuable insights into the mechanism of formation and growth of irradiation-induced defects, such as voids, and their self-organization as void lattices in metallic substrates, such as chromium. We observe that following 5 MeV Fe irradiation, point defects (such as vacancies and interstitials) are generated, which cluster to form voids such as those shown in Fig. 4, characterized by the absence of electron density. This agrees with previously reported studies where the degraded structure of Fe-irradiated Cr is characterized by a relatively large fraction of single or unclustered lattice defects, both vacancies and SIAs, together with several small mobile SIAs clusters⁷³. Further, the evolution of these lattice defects, such as voids in our case, is followed by the presence and growth of interstitial dislocation loops due to the fast diffusion and clustering of SIAs. As explained above, the presence of these dislocation loops is clearly demonstrated by areas of phase shift elucidated by BCDI-based strain mapping. We observe these loops especially in the interfacial region of tensile and compressive strains, as shown by white spheres in strain maps of Fig. 5. It is important to note that an incubation period is necessary for the formation of interstitial dislocation loops or voids⁷⁴. However, in our study, the use of focused beam for ion implantation accelerates such dislocation loop or void formation, thereby shortening the incubation time compared to raster beam approach reported previously⁷⁵.

Once the voids are formed, they act as effective sinks for vacancies, and each void is expected to have a sphere of influence around it that contains a vacancy gradient, since inside that sphere of influence the vacancies tend to become trapped by the void. Once such void growth starts, voids are the dominant defects and evolution of voids continue, leading to the formation of void superlattices⁷⁴. It has been shown that the formation of void lattices tends to mitigate the sphere of influence, thereby retarding further growth of existing voids so that new voids can still nucleate by vacancy clustering. Such enhancement of new

void growth leads to formation of void lattices, which consist of regularly spaced voids.

Such evolution of the void lattice and damaged structure of chromium manifests itself in the form of heterogeneity in the strain distribution in the sample as shown in Fig. 5. Further, such retardment of void growth and its replacement by a self-organized void lattice demonstrates an effective management of radiation-induced defects, which can potentially mitigate radiation-induced damage and lead to improvement in materials performance. For example, it has been demonstrated that self-organized He precipitates form elongated channels in metallic substrates, which ultimately interconnect into percolating ‘vascular’ networks. These vascular networks offer a transformative solution to He-induced damage by enabling in operando outgassing of He and other impurities while maintaining material integrity⁷⁶. Using the BCDI-based strain mapping approach, we can provide a comprehensive understanding of 3D strain and associated defect density as a function of the conditions needed for the formation of superlattices, which results in nanoscale confinement of radiation-induced defects, thus offering a solution where we can drastically reduce and mitigate radiation-induced swelling. However, extensive additional studies are needed to optimize irradiation conditions, minimize radiation-induced defects to determine the minimization of radiation-induced swelling, leading to optimized radiation tolerance in materials.

In summary, we successfully mapped the 3D strain fields using coupled multi-Bragg’s reflections phase retrieval in Fe implanted chromium substrate utilizing BCDI measurements. By considering multiple Bragg reflections, all the voids were mapped, and their 3D morphology and strain were reconstructed. We successfully elucidate the depth dependent heterogeneity in the irradiation-induced strain field of Fe-irradiated chromium. Strain data was utilized to estimate the number density of defects in the irradiated Cr. Findings from BCDI-based 3D mapping were compared with previously reported strain using the TEM technique, demonstrating higher sensitivity of BCDI-based approach. Our results demonstrate that quantitative estimation of 3D strain in irradiated materials using BCDI is a powerful tool to understand fundamental mechanisms of radiation-induced materials degradation in metallic substrates. Further, we demonstrate an approach to correlate radiation-induced defects and associated defect density with microstructural changes induced in metals, such as swelling and embrittlement. Such understanding of degradation of materials in radiation environments via quantification of radiation-induced defects and associated strain is critical for both the design of radiation resistant materials and for the development of predictive models for performance of materials in radiation environments.

METHODS

Sample preparation, ion implantation, and lift-out procedure

Chromium sheets of 99.7% were purchased from American Elements Inc. The cut sample with dimension of $5 \times 5 \times 1$ mm³ was twin-jet electropolished with a solution of 5 vol.% perchloric acid in methanol at ~ -20 °C with an external liquid nitrogen bath. After polishing, samples were repeatedly rinsed in methanol. The sample was implanted with 5 MeV Fe ions at 550 °C at the ion implantation laboratory at Texas A & M University. The implantation was performed using a static defocused beam to avoid suppression of void nucleation, which is commonly observed with rastered beams⁶⁰. The SRIM code³⁸ was used to predict the profile of Fe ion concentration and damage levels in Mo. The Kinchin-Pease method was used for the calculation with a Cr displacement energy of 40 eV. As shown in Fig. 1a, the peak damage occurs at depth of ~ 1.20 μ m, while the peak Fe concentration is located at a depth of ~ 1.36 μ m.

To produce a sufficiently small sample for multi-reflection BCDI, a sub-micron volume ($1.5 \times 1.5 \times 1.5 \mu\text{m}^3$) was lifted out of the 5 MeV Fe ion-implanted Cr sample using FIB milling (Fig. 1(b)–(c)). We adopted the FIB lift-out protocol used by Assefa et al.³³ whereby a single grain was carved out and a 300 nm thick sacrificial platinum cap was deposited over the implanted surface by electron beam assisted deposition. The thickness of the cap was further increased using FIB assisted deposition of platinum (shown in Fig. 1b). This ensures that the Fe ion-implanted surface is not exposed to the energetic gallium ions, which have been shown to result in strain extending over hundreds of nanometers into the substrate material^{32,36}. Afterwards a platinum deposition lift-out sample similar to a TEM or atom probe tomography sample^{77,78} was prepared using a FEI Helios 600 dual-beam (FIB/SEM). A $3 \times 2 \times 2 \mu\text{m}^3$ sized sample was extracted, which was attached to a $3 \times 3 \text{mm}^2$ silicon wafer using platinum deposition (Fig. 1c). The sample was then polished (at lower current and energy of Ga ions to avoid extra damage to the sample) to a size of approximately $1.5 \mu\text{m}$ in each direction. Finally, low energy milling was used to clean off the damage from previous FIB milling, removing 100 nm of material from each side of the sample. Such preparation eliminates most of the damage from previous FIB milling steps.

Data collection and analysis

Micro-Laue diffraction was used to determine the crystallographic orientation of the prepared BCDI sample prior to the collection of multi-reflection BCDI data. This was performed following a recently developed workflow, at 34-ID-C of the Advanced Photon Source using a custom developed code for the analysis of the Laue diffraction data^{79–81}. The UB matrix, which provides the direction and radial position of specific Bragg's peaks⁸², was used to determine the accurate description of the sample orientation on the kinematic mount, which in turn was used to mount and pre-align the sample for multi-reflection BCDI measurements. Multi-reflection BCDI data were collected using a 9.0 keV monochromatic X-ray beam, focused by Kirkpatrick–Baez mirrors as shown in Fig. 2a. To collect suitable coherent X-ray diffraction patterns for reconstruction, the size of X-ray beam should exceed the size of the illuminated crystal. For the chromium crystal of dimension $1.5 \times 1.5 \times 1.5 \mu\text{m}^3$, which exceeds the focused beam size of $600 \times 600 \text{nm}^2$ ($v \times h$); therefore, an unfocused beam size of $30 \times 40 \mu\text{m}^2$ ($v \times h$) was used by opening the slits. Multi-reflection BCDI dataset consisting of four Bragg reflections: (101), (011), (0 $\bar{1}$ 1), and ($\bar{1}$ 01), was measured as the sample was rocked through the Bragg condition to collect over-sampled 3D data in reciprocal space. For each reflection, the crystal was rocked from -0.5° to $+0.5^\circ$ relative to the reflection center in 200 steps with a 1.0 s exposure. The diffraction patterns were collected using a Timepix detector with 256×256 pixels and a pixel size of $55 \times 55 \mu\text{m}^2$ positioned at 2.0 m from the sample. Each scan was repeated six times, aligning the sample to the X-ray beam center before each scan to compensate for any long timescale drift on the quality of data collected during measurements.

Phase retrieval of the BCDI data was carried out using the well-established iterative algorithm implemented in a MATLAB code^{4,83}. The phasing was done in four successive stages following the approach by Hofmann et al.³⁵, whereby the result from a previous cycle was used as a starting seed in the next phasing cycle. Meanwhile, the first cycle was initialized using a random phase guess. The full details of the phase reconstruction are provided in the supplementary methods. Because of the problem of multiple solutions in the phasing of such highly speckled diffraction patterns, we cannot guarantee to have reached a unique solution for each image. Past experience has shown that despite global differences, the number of

density features and their local spacing is qualitatively reproducible, so the counting of defects such as voids should be accurate⁸⁴.

The 3D strain fields tensor (ϵ) and rotation tensor (ω) were calculated by differentiating the displacement field with respect to the sample-frame directions x , y , and z , given as:

$$\text{Elastic normal strain is expressed as } \epsilon_{ij} = \frac{\partial u_i}{\partial r_j} \quad (i, j = x, y, z) \quad (3)$$

$$\text{Elastic shear strains are expressed as } \epsilon_{ij} = \frac{1}{2} \left(\frac{\partial u_i}{\partial r_j} + \frac{\partial u_j}{\partial r_i} \right) \quad (i, j = x, y, z) \quad (4)$$

$$\text{Lattice rotations are expressed as } \omega_{ij} = \frac{1}{2} \left(\frac{\partial u_i}{\partial r_j} - \frac{\partial u_j}{\partial r_i} \right) \quad (i, j = x, y, z) \quad (5)$$

The normal strain with positive values corresponds to tensile strain (swelling) and negative values correspond to compressive strain (contraction). For the rotation term, ω_z is the in-plane rotation or twist about the surface normal z and ω_y and ω_x are the two out-of-plane rotations or tilts about y and x , respectively.

DATA AVAILABILITY

The data discussed in this paper are available upon request to the corresponding authors. Correspondence and requests for materials should be addressed to E.J. (email: ejossou@bnl.gov) and S.K.G. (email: gills@bnl.gov).

Received: 1 July 2022; Accepted: 23 November 2022;

Published online: 22 December 2022

REFERENCES

- Taller, S., VanCoevering, G., Wirth, B. D. & Was, G. S. Predicting structural material degradation in advanced nuclear reactors with ion irradiation. *Sci. Rep.* **11**, 1–14 (2021).
- Li, Z. & Chen, F. Ion beam modification of two-dimensional materials: Characterization, properties, and applications. *Appl. Phys. Rev.* **4**, 011103-1–011103-21 (2017).
- Herbig, C. et al. Xe irradiation of graphene on Ir(111): From trapping to blistering. *Phys. Rev. B: Condens. Matter* **92**, 085429-1–085429-9 (2015).
- Robinson, I. & Harder, R. Coherent X-ray diffraction imaging of strain at the nanoscale. *Nat. Mater.* **8**, 291–298 (2009).
- Doyle, P. J. et al. Evaluation of the effects of neutron irradiation on first-generation corrosion mitigation coatings on SiC for accident-tolerant fuel cladding. *J. Nucl. Mater.* **536**, 152203-1–152203-14 (2020).
- Tang, C., Stueber, M., Seifert, H. J. & Steinbrueck, M. Protective coatings on zirconium-based alloys as accident-tolerant fuel (ATF) claddings. *Corros. Rev.* **35**, 141–165 (2017).
- Rebak, R. B. Current materials in light water reactors. *Why Do We Need A Materials Renewal in Accident Tolerant Materials for Light Water Reactor Fuels?* 1st edn., Vol. 2 (Elsevier, 2020).
- Baron, D. D. & Hallstadius, L. Fuel performance of light water reactors (uranium oxide and MOX). *Compre. Nucl. Mater.* **2**, 481–514 (2012).
- Senchenko, V. N. & Belikov, R. S. Experimental study of thermal expansion of chromium near its melting point. *J. of Phys.:Conf. Ser.* **1787**, 012007 (2021).
- Moore, J. P., Williams, R. K. & Graves, R. S. Thermal conductivity, electrical resistivity, and Seebeck coefficient of high-purity chromium from 280 to 1000 K. *J. Appl. Phys.* **48**, 610–617 (1977).
- Spitz, L. M., Barnard, E. & Brooks, F. D. Neutron capture cross sections of Cr, Mn, Ni, Nb, Ag, In, Sb and Au in the 8 to 120 keV region. *Nucl. Phys.* **A121**, 655–672 (1968).
- Liang, Y. et al. Structure and wear resistance of high hardness Ni-B coatings as alternative for Cr coatings. *Surf. Coat. Technol.* **264**, 80–86 (2015).
- Brachet, J. C. et al. Evaluation of equivalent cladding reacted parameters of Cr-coated claddings oxidized in steam at 1200 °C in relation with oxygen diffusion/partitioning and post-quench ductility. *J. Nucl. Mater.* **533**, 152106-1–152106-16 (2020).
- Wei, T. et al. Microstructure, corrosion resistance and oxidation behavior of Cr-coatings on Zircaloy-4 prepared by vacuum arc plasma deposition. *Corros. Sci.* **158**, 108077-1–108077-12 (2019).

15. Kuprin, A. S. et al. Irradiation resistance of vacuum arc chromium coatings for zirconium alloy fuel claddings. *J. Nucl. Mater.* **510**, 163–167 (2018).
16. Maier, B. R. et al. In situ TEM investigation of irradiation-induced defect formation in cold spray Cr coatings for accident tolerant fuel applications. *J. Nucl. Mater.* **512**, 320–323 (2018).
17. Jiang, L. et al. Effects of ion irradiation on chromium coatings of various thicknesses on a zirconium alloy. *J. Nucl. Mater.* **526**, 1517402-1–1517402-6 (2019).
18. Rajput, M. & Srinivasan, R. Study of transmutation, gas production, and displacement damage in chromium for fusion neutron spectrum. *Ann. Nucl. Energy* **138**, 107187-1–107187-8 (2020).
19. Chen, L., Li, L. Q., Gong, H. R., Fan, J. L. & Li, W. Irradiation effect on mechanical properties of tungsten from molecular dynamic simulation. *Mater. Lett.* **241**, 27–30 (2019).
20. Hardie, C. D., Williams, C. A., Xu, S. & Roberts, S. G. Effects of irradiation temperature and dose rate on the mechanical properties of self-ion implanted Fe and Fe-Cr alloys. *J. Nucl. Mater.* **439**, 33–40 (2013).
21. Das, S. et al. The effect of helium implantation on the deformation behaviour of tungsten: X-ray micro-diffraction and nanoindentation. *Scr. Mater.* **146**, 335–339 (2018).
22. Zinkle, S. J. & Snead, L. L. Opportunities, and limitations for ion beams in radiation effects studies: bridging critical gaps between charged particle and neutron irradiations. *Scr. Mater.* **143**, 154–160 (2018).
23. Jiang, L. et al. Elucidating He-H assisted cavity evolution in alpha Cr under multiple ion beam irradiation. *Scr. Mater.* **187**, 291–295 (2020).
24. Getto, E., Jiao, Z., Monterrosa, A. M., Sun, K. & Was, G. S. Effect of pre-implanted helium on void swelling evolution in self-ion irradiated HT9. *J. Nucl. Mater.* **462**, 458–469 (2015).
25. Fan, Z. et al. From suppressed void growth to significant void swelling in NiCo-FeCr complex concentrated solid-solution alloy. *Materialia* **9**, 100603 (2020).
26. Zhang, J. et al. Effects of grain boundaries on the radiation-induced defects evolution in BCC Fe-Cr alloy: a molecular dynamics study. *Nucl. Mater. Ener.* **22**, 1–7 (2020).
27. Jain, A., Loganathan, S., Kanjilal, D. & Mehta, G. K. High energy heavy ion irradiation of chromium films. *Vacuum* **46**, 369–379 (1995).
28. Kuprin, A. S. et al. Irradiation resistance of chromium coatings for ATFC in the temperature range 300–550 °C. *J. Nucl. Mater.* **549**, 152908-1–152908-6 (2021).
29. Ryabikovskaya, E. et al. Irradiation-induced swelling of pure chromium with 5 MeV Fe ions in the temperature range 450–650 °C. *J. Nucl. Mater.* **543**, 152585-1–152585-9 (2021).
30. Yu, H., Yi, X. & Hofmann, F. 3D reconstruction of the spatial distribution of dislocation loops using an automated stereo-imaging approach. *Ultramicroscopy* **195**, 58–68 (2018).
31. Mason, D. R., Yi, X., Kirk, M. A. & Dudarev, S. L. Elastic trapping of dislocation loops in cascades in ion-irradiated tungsten foils. *J. Phys. Condens. Matter* **26**, 375701-1–375701-18 (2014).
32. Hofmann, F. et al. Glancing-incidence focused ion beam milling: A coherent X-ray diffraction study of 3D nano-scale lattice strains and crystal defects. *Acta Mater.* **154**, 113–123 (2018).
33. Assefa, T. A. et al. Scaling behavior of low-temperature orthorhombic domains in the prototypical high-temperature superconductor $\text{La}_{1.875}\text{Ba}_{0.125}\text{CuO}_4$. *Phys. Rev. B: Condens. Matter* **101**, 054104-1–054104-12 (2020).
34. Newton, M. C., Leake, S. J., Harder, R. & Robinson, I. K. Three-dimensional imaging of strain in a single ZnO nanorod. *Nat. Mater.* **9**, 120–124 (2010).
35. Hofmann, F. et al. Nanoscale imaging of the full strain tensor of specific dislocations extracted from a bulk sample. *Phys. Rev. Mater.* **4**, 013801–013801-12 (2020).
36. Hofmann, F. et al. 3D lattice distortions and defect structures in ion-implanted nano-crystals. *Sci. Rep.* **7**, 1–10 (2017).
37. Li, Z. Z. et al. Investigating the formation mechanism of void lattice in tungsten under neutron irradiation: from collision cascades to ordered nanovoids. *Acta Mater.* **219**, 117239-1–117239-15 (2021).
38. Ziegler, J. F., Ziegler, M. D. & Biersack, J. P. SRIM-the stopping and range of ions in matter (2010). *Nucl. Instrum. Methods Phys. Res. B* **268**, 1818–1823 (2010).
39. Abuin, M. et al. Coherent X-ray imaging of CO-adsorption-induced structural changes in Pt nanoparticles: implications for catalysis. *ACS Appl. Nano Mater.* **2**, 4818–4824 (2019).
40. Estandarte, A. K. C. et al. Operando Bragg coherent diffraction imaging of $\text{LiNi}_{0.8}\text{Mn}_{0.1}\text{Co}_{0.1}\text{O}_2$ primary particles within commercially printed NMC811 electrode sheets. *ACS Nano* **15**, 1321–1330 (2021).
41. Clark, J. N. et al. Three-dimensional imaging of dislocation propagation during crystal growth and dissolution. *Nat. Mater.* **14**, 780–784 (2015).
42. Phillips, N. W. et al. Nanoscale lattice strains in self-ion implanted tungsten. *Acta Mater.* **195**, 219–228 (2020).
43. Wang, T., Kim, H., Garner, F. A., Peddicord, K. L. & Shao, L. The effect of internal free surfaces on void swelling of irradiated pure iron containing subsurface trenches. *Crystals* **9**, 1–11 (2019).
44. Pickering, E. J. et al. High-entropy alloys for advanced nuclear applications. *Entropy* **23**, 1–28 (2021).
45. Tissot, O., Pareige, C., Meslin, E., Décamps, B. & Henry, J. Influence of injected interstitials on α' precipitation in Fe-Cr alloys under self-ion irradiation. *Mater. Res. Lett.* **5**, 117–123 (2017).
46. Ulvestad, A. et al. Identifying defects with guided algorithms in Bragg coherent diffractive imaging. *Sci. Rep.* **7**, 1–9 (2017).
47. Ulvestad, A., Menickelly, M. & Wild, S. M. Accurate, rapid identification of dislocation lines in coherent diffractive imaging via a min-max optimization formulation. *AIP Adv.* **8**, 015114-1–015114-6 (2018).
48. Lou, C., Yu, J., Liu, L., Ren, Y. & Zhang, X. {10–12} twin nucleation induced by FIB micro-stress in magnesium single crystal. *Mater. Lett.* **210**, 139–142 (2018).
49. Kiener, D., Motz, C., Rester, M., Jenko, M. & Dehm, G. FIB damage of Cu and possible consequences for miniaturized mechanical tests. *Mater. Sci. Eng. A* **459**, 262–272 (2007).
50. Dennett, C. A. et al. Detecting self-ion irradiation-induced void swelling in pure copper using transient grating spectroscopy. *Acta Mater.* **145**, 496–503 (2018).
51. Derlet, P. M. & Dudarev, S. L. Microscopic structure of a heavily irradiated material. *Phys. Rev. Mater.* **4**, 023605-1–023605-20 (2020).
52. Song, K. et al. Characterizing ion-irradiated FeCr: hardness, thermal diffusivity and lattice strain. *Acta Mater.* **201**, 535–546 (2020).
53. Dudarev, S. L., Mason, D. R., Tarleton, E., Ma, P. W. & Sand, A. E. A multi-scale model for stresses, strains and swelling of reactor components under irradiation. *Nucl. Fus.* **58**, 126002-1–126002-16 (2018).
54. Ma, P. W. & Dudarev, S. L. Effect of stress on vacancy formation and migration in body-centered cubic metals. *Phys. Rev. Mater.* **3**, 063601-1–063601-12 (2019).
55. Cui, L. J. et al. TEM characterization of irradiation-induced dislocation loops and voids in ion-irradiated pure chromium. *J. Nucl. Mater.* **569**, 153920-1–153920-16 (2022).
56. Bryk, V. V., Voyevodin, V. N., Neklyudov, I. M. & Rakitskij, A. N. Microstructure investigation of Cr and Cr alloys irradiated with heavy ions. *J. Nucl. Mater.* **225**, 146–153 (1995).
57. Getto, E. et al. Void swelling and microstructure evolution at very high damage level in self-ion irradiated ferritic-martensitic steels. *J. Nucl. Mater.* **480**, 159–176 (2016).
58. Hofmann, F. et al. Lattice swelling and modulus change in a helium-implanted tungsten alloy: X-ray micro-diffraction, surface acoustic wave measurements, and multiscale modelling. *Acta Mater.* **89**, 352–363 (2015).
59. Ma, P. W. & Dudarev, S. L. Universality of point defect structure in body-centered cubic metals. *Phys. Rev. Mater.* **3**, 013605-1–013605-16 (2019).
60. Ipatova, I. et al. Radiation-induced void formation and ordering in Ta-W alloys. *J. Nucl. Mater.* **495**, 343–350 (2017).
61. Möller, J. J. & Bitzek, E. BDA: a novel method for identifying defects in body-centered cubic crystals. *MethodsX* **3**, 279–288 (2016).
62. Short, M. P., Gaston, D. R., Jin, M., Shao, L. & Garner, F. A. Modeling injected interstitial effects on void swelling in self-ion irradiation experiments. *J. Nucl. Mater.* **471**, 200–207 (2016).
63. Shao, L. et al. Effect of defect imbalance on void swelling distributions produced in pure iron irradiated with 3.5 MeV self-ions. *J. Nucl. Mater.* **453**, 176–181 (2014).
64. Agarwal, S. et al. A new mechanism for void-cascade interaction from non-destructive depth-resolved atomic-scale measurements of ion irradiation-induced defects in Fe. *Sci. Adv.* **6**, 1–6 (2020).
65. Ayanoglu, M. & Motta, A. T. Void shrinkage in 21Cr32Ni austenitic model alloy during in-situ ion irradiation. *J. Nucl. Mater.* **543**, 152636-1–152636-7 (2021).
66. Zhou, Z., Dudarev, S. L., Jenkins, M. L., Sutton, A. P. & Kirk, M. A. Diffraction imaging and diffuse scattering by small dislocation loops. *J. Nucl. Mater.* **367–370 A**, 305–310 (2007).
67. Yi, X. et al. Direct observation of size scaling and elastic interaction between nano-scale defects in collision cascades. *EPL* **110**, 36001-p1–36001-p6 (2015).
68. Zhang, Y., Bai, X. M., Tonks, M. R. & Biner, S. B. Formation of prismatic loops from C15 Laves phase interstitial clusters in body-centered cubic iron. *Scr. Mater.* **98**, 5–8 (2015).
69. Osetsky, Y. N., Bacon, D. J., Serra, A., Singh, B. N. & Golubov, S. I. Stability and mobility of defect clusters and dislocation loops in metals. *J. Nucl. Mater.* **276**, 65–77 (2000).
70. Hirst, C. A. et al. Revealing hidden defects through stored energy measurements of radiation damage. *Sci. Adv.* **8**, 1–9 (2022).
71. Weiß, O. J., Gaganidze, E. & Aktaa, J. Quantitative characterization of micro-structural defects in up to 32 dpa neutron irradiated EUROFER97. *J. Nucl. Mater.* **426**, 52–58 (2012).
72. Reza, A., Yu, H., Mizohata, K. & Hofmann, F. Thermal diffusivity degradation and point defect density in self-ion implanted tungsten. *Acta Mater.* **193**, 270–279 (2020).
73. Singh, B. N. & Evans, J. H. Significant differences in defect accumulation behavior between fcc and bcc crystals under cascade damage conditions. *J. Nucl. Mater.* **226**, 277–285 (1995).

74. Norris, D. I. R. Voids in irradiated metals (Part II). *Radiat. Eff.* **15**, 1–22 (1972).
75. Getto, E., Jiao, Z., Monterrosa, A. M., Sun, K. & Was, G. S. Effect of irradiation mode on the microstructure of self-ion irradiated ferritic-martensitic alloys. *J. Nucl. Mater.* **465**, 116–126 (2015).
76. Chen, D. et al. Self-organization of helium precipitates into elongated channels within metal nanolayers. *Sci. Adv.* **3**, 1–7 (2017).
77. Meisnar, M., Vilalta-Clemente, A., Moody, M., Arioka, K. & Lozano-Perez, S. A mechanistic study of the temperature dependence of the stress corrosion crack growth rate in SUS316 stainless steels exposed to PWR primary water. *Acta Mater.* **114**, 15–24 (2016).
78. Meisnar, M., Moody, M. & Lozano-Perez, S. Atom probe tomography of stress corrosion crack tips in SUS316 stainless steels. *Corros. Sci.* **98**, 661–671 (2015).
79. Larson, B. C., Yang, W., Ice, G. E., Budai, J. D. & Tischler, J. Z. Three-dimensional X-ray structural microscopy with submicrometre resolution. *Nature* **415**, 887–890 (2002).
80. Liu, W. et al. The three-dimensional X-ray crystal microscope: a new tool for materials characterization. *Metall. Mater. Trans. A* **35**, 1963–1967 (2004).
81. Pateras, A. et al. Combining Laue diffraction with Bragg coherent diffraction imaging at 34-ID-C. *J. Synchrotron Radiat.* **27**, 1430–1437 (2020).
82. Hofmann, F. et al. Micro-beam Laue alignment of multi-reflection Bragg coherent diffraction imaging measurements. *J. Synchrotron Radiat.* **24**, 1048–1055 (2017).
83. Robinson, I. K., Vartanyants, I. A., Williams, G. J., Pfeifer, M. A. & Pitney, J. A. Reconstruction of the shapes of gold nanocrystals using coherent x-ray diffraction. *Phys. Rev. Lett.* **87**, 195505-1–195505-4 (2001).
84. Robinson, I. et al. Domain texture of the orthorhombic phase of $\text{La}_{2-x}\text{Ba}_x\text{CuO}_4$. *J. Supercond. Nov. Magn.* **33**, 99–106 (2020).

ACKNOWLEDGEMENTS

This work was sponsored by the U.S. Department of Energy (DOE), Office of Science, Basic Energy Sciences (BES), Materials Sciences and Engineering Division under FWP #C000-14-003. E.J. would like to thank Prof. F. Hofmann and D. Yang for their insightful discussion on the phase retrieval code. T.A. would like to acknowledge support by the Department of Energy, Office of Science, Basic Energy Sciences, Materials Sciences, and Engineering Division, under Contract DE-AC02-76SF00515. C.S. would like to thank Prof. Lin Shao for sharing the Cr sample with us. The ion irradiation was supported by Nuclear Science User Facility RTE project 1799. The focused ion beam sample preparation used the resources of the Center for Functional Nanomaterials, which is a US DOE Office of Science Facility, at BNL under Contract No. DE-SC0012704. The experiments were carried out at Advanced Photon Source (APS) beamline 34-ID-C, and the APS was supported by the US Department of Energy, Office of Science, Office of Basic Energy Sciences, under Contract No. DE-AC02-06CH11357. The beamline 34-ID-C was built with US National Science Foundation

Grant No. NSF-DMR 9724294 Development of a Coherent X-Ray Diffraction Instrument 09/15/1997.

AUTHOR CONTRIBUTIONS

E.J., S.K.G., and L.E. designed the project. C.S., J.G., and K.K. irradiated and prepared the samples for synchrotron-based experiments. E.J., T.A.A., A.F.S., S.K.G., W.C., I.K.R., and R.H. were involved in the coherent diffraction experiment at APS. E.J. analyzed the data with the help of T.A.A., A.F.S., and L.W. while E.J. wrote the paper with the help of all co-authors.

COMPETING INTERESTS

The authors declare no competing interests.

ADDITIONAL INFORMATION

Supplementary information The online version contains supplementary material available at <https://doi.org/10.1038/s41529-022-00311-8>.

Correspondence and requests for materials should be addressed to Eric Moore Jossou or Simerjeet K. Gill.

Reprints and permission information is available at <http://www.nature.com/reprints>

Publisher's note Springer Nature remains neutral with regard to jurisdictional claims in published maps and institutional affiliations.



Open Access This article is licensed under a Creative Commons Attribution 4.0 International License, which permits use, sharing, adaptation, distribution and reproduction in any medium or format, as long as you give appropriate credit to the original author(s) and the source, provide a link to the Creative Commons license, and indicate if changes were made. The images or other third party material in this article are included in the article's Creative Commons license, unless indicated otherwise in a credit line to the material. If material is not included in the article's Creative Commons license and your intended use is not permitted by statutory regulation or exceeds the permitted use, you will need to obtain permission directly from the copyright holder. To view a copy of this license, visit <http://creativecommons.org/licenses/by/4.0/>.

© The Author(s) 2022